Modeling, measurements, and analysis of x-ray emission from 0.26-μm-laser-irradiated gold disks

W. C. Mead and E. K. Stover
Los Alamos National Laboratory, Los Alamos, New Mexico 87545

R. L. Kauffman, H. N. Kornblum, and B. F. Lasinski
Lawrence Livermore National Laboratory, Livermore, California 94550
(Received 10 August 1987; revised manuscript received 18 July 1988)

We present modeling, measurements and analysis that extend our understanding of laser-plasma coupling and x-ray conversion processes to shorter laser wavelengths at kilojoule energies. We have studied the x-ray emission from gold-disk targets irradiated at 0.26-μm wavelength, using 0.5–1.5-kJ, 1-ns full width at half maximum Gaussian pulses at intensities of 1×10^{14}–2×10^{15} W/cm^2. We interpret measurements of the absolute broadband x-ray spectrum, the time history of sub-keV x-ray emission flux, and the broadband hard-x-ray spectrum. We find negligible hot-electron levels ($<10^{-3}E_{\rm inc}$). We infer increased conversion of incident light to soft x rays (72%±15% at 1×10^{14} and 38%±12% at 2×10^{15}), compared with longer wavelengths, as predicted. We find good overall agreement between the modeling and the data, but identify some areas that need to be better understood, including certain aspects of the x-ray emission spectrum and the decay rate of the emission pulse.

I. INTRODUCTION

The interaction of submicrometer laser light with high-Z plasmas presents a fascinating, complex interplay of diverse physical processes. Moreover, the efficiency of conversion of submicrometer laser light into soft x rays is important in determining the performance of x-ray driven inertial confinement fusion (ICF) targets.[1] As a result, considerable effort has been devoted to understanding the mechanisms involved in laser-plasma coupling and x-ray conversion.

When a laser is incident on a high-Z target at high intensities, a plasma corona quickly forms. For submicrometer-wavelength laser light at peak intensities below about 10^{15} W/cm^2 and for high-Z target plasmas, the light is efficiently absorbed near or below its critical density by strong inverse bremsstrahlung collisional absorption. Inverse bremsstrahlung primarily heats the bulk of the plasma electron distribution, leading to temperatures of several kilo-electron-volts (keV). The energy deposited into the electrons is then transported to the unheated, higher-density regions of the plasma, converted by electron-ion collisions into excitations that lead to x-ray emission, and converted hydrodynamically into convecting ion kinetic energy. The competition among these energy transport and conversion processes depends on the temperatures, scalelengths, and charge states of the plasma, which in turn are self-consistently determined by the irradiation conditions, i.e., intensity, pulse width, and spot diameter, and the laser-plasma coupling processes. Although a detailed understanding of these processes can best be obtained using computer simulations, behavior of the dominant processes can be readily understood by consideration of their basic scaling relationships, to which we shall return in a moment.

The earliest reported observations of laser-plasma coupling for high-intensity irradiations of high-Z targets were those of Shay *et al.*[2] at 1.06-μm wavelength. They reported efficient conversion of laser light to x rays and noted nonuniform x-ray-emission structures that correspond with structures in the incident laser beam. Rosen *et al.*[3] used greatly improved modeling and diagnostics, and were the first to discuss the importance of both thermal transport inhibition and non-local-thermodynamic-equilibrium (non-LTE) atomic physics in modeling high-Z target irradiations at 1.06-μm wavelength, for intensities of about 3×10^{14} W/cm^2 or higher. They also showed the first accurate scaling measurements for the intensity dependence of x-ray conversion processes, showing that x-ray conversion efficiency decreases as laser intensity increases. Nishimura *et al.*[4] performed experimental wavelength scaling studies and reported high-Z target measurements showing x-ray conversion efficiency increasing with shorter laser wavelength in the intensity range of 10^{13}–10^{14} W/cm^2. Their work also included high-Z thin-foil burn-through measurements. Mead *et al.*[5] reported extensive measurements and modeling of 0.53-μm irradiations of gold- and titanium-disk targets. They, too, found that x-ray conversion efficiency for gold-disk targets increased at shorter wavelengths. Further, Mead *et al.* found that the wavelength scaling agreed with computer hydrodynamics code predictions (using modeling similar to that of Rosen *et al.*), except at intensities below 3×10^{14} W/cm^2, where experiments suggested a rolloff, while calculations predicted continued increase.

Recently, experimental and modeling studies of laser-plasma coupling and x-ray conversion in high-Z plasmas have been extended and refined at several laboratories. Various spectrometers have been developed and used to

obtain high-resolution x-ray spectra,[6-9] allowing study of the complex line structures of emission from high-Z plasmas. Measurements have shown excess emission from gold plasmas in the 100–300-eV spectral region, compared with hydrodynamics code modeling including average-atom non-LTE atomic physics.[6,8,9] The Z dependence of emission has also been observed in more detail.[6,10] Kodama *et al.*[11] performed wavelength scaling studies at 1.05, 0.53, and 0.26 μm, using laser energies of about 10 J. Goldstone *et al.*[9] presented detailed studies of the "dynamics" of high-Z plasmas (i.e., hydrodynamic scales, energy penetration depths, and time dependence of emission), using layered gold-on-CH spherical targets. Studies of laser-target interactions have also been performed in high-Z laser-heated cavities.[7,12]

Theoretical and computational modeling of high-Z plasmas has been developed and widely applied, as well. As mentioned above, the effects of non-LTE atomic and radiation physics have been found to be important in determining plasma and emission conditions.[3,5,6,8] Radiation waves penetrating into the dense portion of laser-irradiated targets have been studied computationally.[13] Goldman and Mead studied the scaling of high-Z laser-target interactions to large laser and plasma sizes,[14] predicting that the steep plasma profiles responsible for non-LTE effects in current experimental plasmas will persist for high-intensity laser interactions with large, high-Z plasmas of interest in future ICF applications.

As background to the present work, let us summarize the status of x-ray conversion efficiency calculations and data[3-5] at the time when we began this work.[15] The total x-ray conversion efficiency ($\eta_t = E_{\rm rad}/E_{\rm abs}$, where $E_{\rm rad}$ is the total radiated energy and $E_{\rm abs}$ is the absorbed energy) is predicted by LASNEX (Ref. 16) hydrodynamic code calculations to increase as $I\lambda^2$ decreases. Measured conversion efficiencies agreed well (for the higher-intensity, longer-wavelength points) with the power-law fit to LASNEX calculations using inhibited electron transport. However, at lower intensities and shorter wavelengths, measured conversion efficiencies were below those predicted by as much as 50%. At the outset of this work, the wavelength scaling of this discrepancy between experiment and calculations was not clear.

In the work reported here, we extend wavelength-scaling studies to 0.26-μm wavelength at kilojoule energies, making use of measurements performed at the Lawrence Livermore National Laboratory's Novette laser, hydrodynamics code calculations, and extensive analysis of the results. The measurements include time-integrated and time-resolved observations of the sub-keV x-ray region, together with time-integrated measurements of the multi-keV x rays generated in the hot corona. The experiments used 0.5–1.5-kJ, 1-ns Gaussian laser pulses at peak intensities from 1×10^{14}–2×10^{15} W/cm^2. We have analyzed the soft-x-ray spectra extensively, since they give important clues to plasma conditions and, further, affect the behavior of x-ray-driven ICF targets.

The key physical processes in these collisional, high-Z plasmas are inverse bremsstrahlung laser absorption, hydrodynamics, non-LTE atomic and radiation physics, and energy transport. Inverse bremsstrahlung absorption is a three-body collisional process, and the photon absorption opacity scales as

$$Z^2 n_e n_i T_e^{-3/2}[1-(n_e/n_c)]^{-1/2} .$$

Thus absorption occurs most strongly at high electron (n_e) and ion (n_i) densities, low electron temperatures (T_e), and at electron densities near the laser's critical density (n_c). The radiation emission processes are most efficient where bound-bound transitions in gold ions are strongly excited by collisions with the plasma electrons, i.e., at the highest densities at which the few-hundred-eV temperatures needed to excite gold N-shell transitions ($\Delta E_{4-5} \simeq 800$ eV) are available. The emission processes are strongly non-LTE, particularly at high intensities, since, as discussed below, the plasma develops steep density and temperature profiles, so that the gold ions sweep rapidly ($\sim$5–10 ps) through regions of violently changing plasma conditions. Radiation transport can be important when emission processes are efficient enough to convert large fractions of the absorbed laser energy into photons, which generally have longer mean free paths (MFP) than electrons in these plasmas. Energy transport by electron conduction is most important where temperatures are higher (the electron mean free path scales as $\lambda_{\rm MFP} \sim T_e^2$), x-ray-emission processes are too weak to convert the absorbed energy locally, and where other processes create steep gradients (e.g., where the laser energy deposits strongly near the critical density surface). It would be useful to combine this physics in an analytic model for high-Z plasmas, although it is difficult to treat the various nonlinear processes involved.

Using computer hydrodynamics code simulations, which include models for these processes, we can see their interplay and their roles in controlling the conversion of submicrometer laser light into x rays. This interplay is illustrated in the calculated plasma profiles shown in Fig. 1 at the peak of a 1-ns Gaussian laser pulse. Figure 1(a) shows the plasma profiles for the low-intensity regime, while Fig. 1(b) shows the same for the high-intensity regime. At low intensities, the underdense plasma can radiate rapidly enough to remove the deposited laser energy locally. The calculations predict a cool corona with an extended absorption and emission region. Pressure gradients and hydrodynamic losses are relatively small. Calculated x-ray conversion efficiencies are high. At higher intensities, radiation from the underdense plasma can no longer cool the corona as rapidly as the laser deposits its energy. As a result, the corona becomes much hotter and electron transport carries some of the energy into the overdense plasma where radiation processes are more rapid. Since inverse bremsstrahlung absorption is less efficient in the hot underdense plasma, the laser deposits its energy most efficiently in the cooler, denser plasma near the critical surface. Electron mean free paths are short in this region of the plasma, so the temperature, density, and velocity profiles become steep near critical. Higher corona temperatures and steeper gradients increase the energy transfer to hydrodynamic

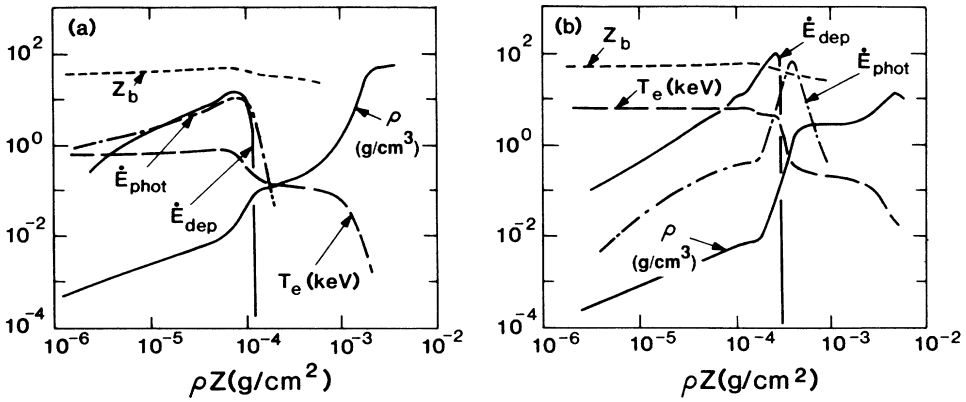

FIG. 1. Calculated plasma profiles for gold-disk targets at 0.26-μm wavelength, about 1-kJ energy, and 1-ns pulse duration. Curves show the average ionization state (Z_b), plasma density (ρ), electron temperature (T_e), laser specific deposition rate ($\dot{E}_{dep}$), and net photon emission rate ($\dot{E}_{phot}$). Laser enters from the left. The profile characteristics change significantly between (a) 10^{14} and (b) 10^{15} W/cm^2. The lower-intensity case shows extended laser-absorption and x-ray-emission regions, while the gradients are steep around the critical surface and the x-ray emission from plasma above the critical density plays an important role in the higher intensity case.

blow-off, while the need to transport energy into the overdense plasma before it can radiate further reduces the energy available for radiation. Thus the x-ray conversion efficiency is reduced at higher intensities.

This paper is organized as follows. In Sec. II we discuss the modeling used in this work, and present a few predictions that are needed for analysis of the measurements. Section III describes details of the experiment. Section IV presents the soft x-ray data and analysis. Section V discusses the multi-keV x-ray results. Finally, our conclusions are presented in Sec. VI.

II. MODELING AND PREDICTIONS

In this section we discuss details of the calculational modeling and present predictions of the modeling that are used in the analysis of the experiment.

A. Modeling details

The modeling assumptions used in the LASNEX (Ref. 16) calculations presented here correspond closely with those used previously to model successfully the observed high-Z laser-plasma behavior.[3,5] As discussed above, the dominant processes in high-Z laser-plasma coupling are hydrodynamics, laser absorption, and non-LTE atomic and radiation physics, with electron thermal conduction also playing a key role at high intensities.

The calculations performed for this work used Lagrangian hydrodynamics with r-z cylindrical coordinates (axisymmetry assumed about the z axis). Plasma pressure, energy, and other thermodynamic quantities were calculated for each zone from a tabulated equation of state, until plasma temperatures exceeded 20 eV.

Laser energy was propagated according to geometrical optics using ray tracing, with inverse bremsstrahlung absorption computed along the ray trajectories. The modeling neglected stimulated Brillouin scattering, which should be negligible[5] at our modest values of $I\lambda^2$. For historical reasons,[5] we modeled collective absorption processes using a 10 % "dump" at the critical surface in some of the calculations. However, this had little effect on the results, and the measurements implied negligible hot-electron generation by collective plasma processes (see Sec. V).

A time-dependent solution of the hydrogenic non-LTE collisional and radiative rate equations supplied rates for ionization, atomic transitions, and radiation emission, and provided most of the thermodynamic quantities, for all zones in the calculations above 20 eV in temperature. In LASNEX, a frequency-dependent "emission opacity" is defined (by analogy with LTE) as the "opacity" by which the local-Planckian photon density must be multiplied to obtain the (non-LTE) emission. In this work, as discussed below, we have found it convenient at times to use a frequency-independent emission opacity multiplier ϵ_r to alter the calculated overall emission levels. Non-LTE effects are important, particularly in the steepened plasmas associated with the higher intensities in this work.

At the higher irradiation intensities, electron thermal conduction becomes important as a mechanism to transport the deposited energy into the overdense plasma. Electron transport was performed using flux-limited diffusion of a single Maxwellian thermal electron group. Except where otherwise noted, we used an intermediate flux-limit value,[3,5,17,18] $f_e=0.05$, which we find fits the current measurements with the best overall consistency. The effect of the flux limit and the appropriate range of values for modeling this experiment are discussed below.

For this work, thermoelectric magnetic fields and multigroup hot-electron modeling were neglected. Previous work[5,18] indicates that these features play modest roles in determining the overall energetics and conditions of high-Z, short-wavelength laser-produced plasmas. As discussed in Sec. V, the hard-x-ray spectrum suggests

negligible hot-electron populations, even at the highest intensities investigated here, 2×10^{15} W/cm^2.

Calculations for this work were performed in both one- (1D) and two-dimensional (2D) geometries. Many of the calculations used to test the numerics, assess physics sensitivities, and analyze the experiment were performed using a 1D model that agreed fairly well with the 2D calculations. We chose a 1D geometry that preserved the spatially averaged laser intensity, and approximated the blow-off divergence via a 15° expansion angle. The effects of divergence and the differences between 1D and 2D calculations are discussed in Sec. II B.

We performed zoning studies for each of the intensities used in this work. We found no difficulty in resolving the 1×10^{14}- and 3×10^{14}-W/cm^2 cases to a convergence of better than 5% in quantities of interest. However, for the calculations at 2×10^{15} W/cm^2, we found that the cost of obtaining such resolution for the strongly steepened profiles was too high. For this intensity, we therefore used a zoning study to determine the zero-zone-size asymptotic value of the predicted x-ray conversion efficiency.[5] Then, for an affordable zoning, we adjusted the emission opacity multiplier ϵ_r to the value required to reproduce the asymptotic conversion efficiency, namely, $\epsilon_r=0.7$. This approximation does not fully resolve various details of the physics, and, as a result, leads to slight errors in details such as the x-ray spectral shape. This is discussed further in Sec. IV B.

B. Predictions for 0.26-μm irradiations

Calculated absorption depends on many aspects of the modeling: the inverse-bremsstrahlung-absorption model, the electron-transport model, the calculated average ionization state, and, of course, the irradiation conditions. For the 1×10^{14}-W/cm^2 case, the calculated absorption is nearly 100%, since the plasma is sufficiently large and cool to provide many absorption lengths. In this case, modeling details mainly determine where in the plasma the energy is absorbed, rather than changing the magnitude of the absorption. For the 2×10^{15}-W/cm^2 case, the calculated absorption using the reference model ($f_e=0.05$) is 80%. Here, the absorption is more sensitive to modeling details. For example, varying f_e changes the absorption considerably, increasing the absorption as f_e is increased. The absorption could also be reduced by stimulated Brillouin scattering, but we expect this process to be weak at the modest $I\lambda^2$ of these 0.26-μm irradiations,[5] and have neglected it here.

Two-dimensional calculations were performed to evaluate the effects of lateral thermal transport and divergence of the hydrodynamic blow-off, and to calculate the x-ray angular distributions. Figure 2 shows a sample mesh and ray trace for a 2×10^{15}-W/cm^2 2D calculation at the time of peak laser power. The laser, represented in the calculations by 100–400 rays, is incident from the right. We have neglected the 30° target tilt (discussed below, Sec. III, Fig. 4), since similar calculations showed negligible effects for such a small change in angle of incidence. The peak electron temperature in the plasma is 4.8 keV in this 2D calculation.

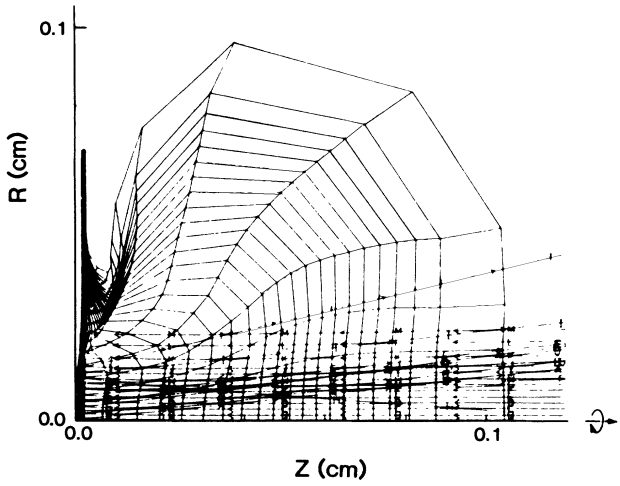

FIG. 2. Snapshot of 2D LASNEX calculation at the time of the peak of the laser pulse for $\lambda_L=0.26$ μm, $\tau_L=1$ ns, $E_L=1.3$ kJ, and $I_L=2\times10^{15}$ W/cm^2, using $f_e=0.05$. Lagrangian mesh and laser rays (incident from the right) are shown. Remnant of the original disk target is seen at the left. Plasma plume expansion shows divergence of the flow away from the laser spot.

The 2D calculations suggest that lateral thermal transport is energetically negligible for the parameters of this work. This is supported by the observed x-ray emission images, presented in Sec. III. For the lowest intensity case, the x-ray images reproduced details of known beam-structure features such as the laser-disk split and the framework supporting the frequency conversion crystals. For the highest-intensity case, the x-ray image on target corresponded with the expected beam spot size.

One- and two-dimensional calculations were compared to evaluate the effects of divergence of the hydrodynamic blow-off. As in previous related work,[3,5,18] the blow-off plasma does diverge in the 1D calculations using 15° divergence angle, causing some additional hydrodynamic cooling of the corona, compared with that which is calculated in 1D cylindrical geometry (blow-off constrained to remain planar). Additional expansion in the 2D calculations leads to about 20–30 % reduction (relative to planar calculations) in peak corona temperatures for the 1×10^{14}- and 2×10^{15}-W/cm^2 cases. Using our 1D divergent geometry, we could account for about half of the full 2D divergence effect, leading to a mock-up of the 2D calculation that was accurate to within about 10% in peak electron temperature and 2% in x-ray conversion efficiency, and that can be used for systematic parameter studies in various cases of interest. Below, we discuss two areas that are particularly sensitive to details of the modeling, and for which 1D modeling is inadequate: the sensitivity of the decay of the x-ray-emission pulse to plasma expansion (Sec. IV E), and the sensitivity of the hard-x-ray spectrum to small changes in corona temperature (Sec. V).

We wish to infer the total x-ray emission from the soft-x-ray measurements, but these were performed at only one angle: 60° with respect to the target normal. We must therefore rely on calculated x-ray angular distri-

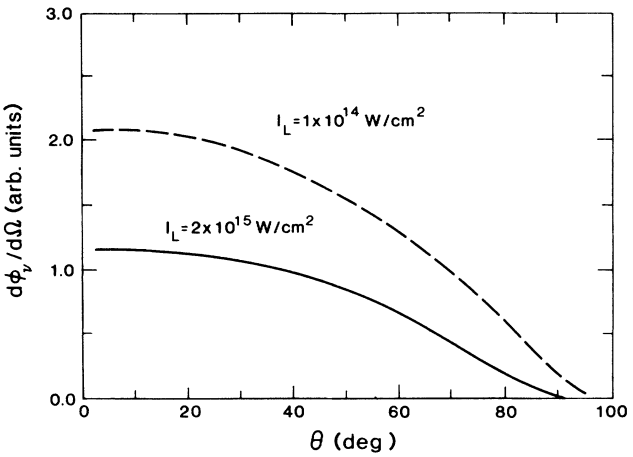

FIG. 3. X-ray-emission angular distributions obtained from 2D LASNEX calculations. θ is the angle from the target normal. These distributions have been used to infer total yields from the single-angle x-ray measurements.

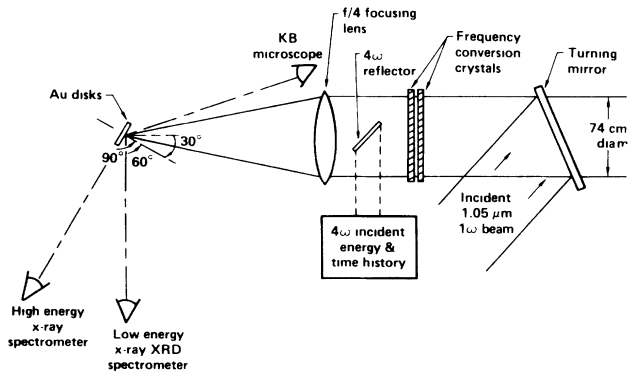

FIG. 4. Schematic of this experiment. Irradiations used 0.26-μm light in 1-ns, 0.5–1.5-kJ pulses to obtain intensities of 1×10^{14} to 2×10^{15} W/cm^2. The Au-disk target was tilted at 30° to the incident beam direction, allowing the soft x rays to be observed by several diagnostics at 60° to the target normal.

butions. This procedure has been verified in previous work[5] to within experimental accuracy (about 15%). Angular distributions obtained from TDG post-processing[2] of the 2D LASNEX calculations are shown in Fig. 3. We calculate angle-integration factors of 6.16 and 5.91 for the 60° flux measurements for the 1×10^{14}- and 2×10^{15}-W/cm^2 cases, respectively. Note that these factors are within a few per cent of the factor 2π expected for a $\cos\theta$ angular distribution. This is a result of our choice of the 60° measuring angle and the fact that the calculated distribution is $\sim(\cos\theta)^{0.6-1.0}$. For the analysis below, we have used the LASNEX-calculated integration factors.

III. EXPERIMENT

A schematic of the experimental arrangement is shown in Fig. 4. The 1.05-μm laser beam was converted to its fourth harmonic, 0.26 μm, by repeated nonlinear doubling using potassium diphosphate (KDP) crystals. Laser output was typically 7 kJ at 1.05 μm, which yielded up to 1.7 kJ of frequency-quadrupled energy on target. The 0.26-μm beam was focused onto the target using a quartz $f/4$ lens. Residual 1.05- and 0.53-μm light was effectively eliminated from the target by using a beam-center stop that, together with the chromatic aberration of the focusing lens, created a shadow of about 5 mm diameter at these two wavelengths around the position of the 0.26-μm focus.

Incident 0.26-μm energy and pulse shape were determined using a beam pick-off that extracted the entire central segment of the frequency-conversion array, $\frac{1}{25}$ of the total beam area. Before the experiments, the beam pick-off was calibrated against the total beam-on-target energy measured using a 74-cm calorimeter beyond the focus in the target chamber. Accuracy and repeatability of the energy calibration was about 15% rms. The laser pulse temporal profile was nearly Gaussian, with a 1-ns full width at half maximum (FWHM).

The irradiation intensity was varied by displacing the focusing lens to change the spot size on the target. Spot diameters ranged from 1.4 mm for the 1×10^{14}-W/cm^2 irradiations, to about 0.3 mm for the 2×10^{15}-W/cm^2 cases. On simple grounds, one can suspect that the expansions in these irradiations could be significantly affected by two-dimensional effects: taking a sound speed of roughly 2×10^7 cm/s, together with the pulse width of 1 ns, a characteristic expansion distance should be about 0.2 mm. Thus the high-intensity case could easily be affected by the two dimensionality of the blow-off, as discussed in Sec. II.

Two target types were used. The targets used for small-spot-size irradiations were gold disks, about 1.3 mm in diameter. For the large-spot-size irradiations, we used square gold plates, 5 mm on a side. All targets were 4.8 μm thick, which is large enough to prevent significant heating of the rear target surface or significant target acceleration. The targets were generally tilted by 30° relative to the laser-beam's axis, to permit the soft x-ray diagnostics to view the target surface at 60° to the normal.

The main diagnostics used in these measurements are shown schematically in Fig. 4. They include an x-ray microscope (with four broadband channels in the 1–3-keV range), the ten-channel Dante x-ray-diode (XRD) soft-x-ray detector system,[3,19,20] a grating streak-camera spectrograph,[21] and a multichannel hard-x-ray filter-fluorescer system (FFLEX).[3] The angle of each of these detector systems to the target normal is given in the figure.

Characteristics of the laser beams on target were inferred from images of the target x-ray emission. While this approach is less desirable than optical equivalent-plane measurements as a result of its dependence upon target physics, nonetheless, a reasonable knowledge of the beam characteristics can be obtained. Figure 5 shows x-ray images of gold-disk irradiations at the two extreme spot sizes used in this work. The large spot, corresponding with the 1×10^{14} W/cm^2 irradiations, clearly shows a sharp dark band, corresponding to the occlusion produced by the segmented disks used in the final amplifiers of Novette. Strong small-scale structures can be clearly

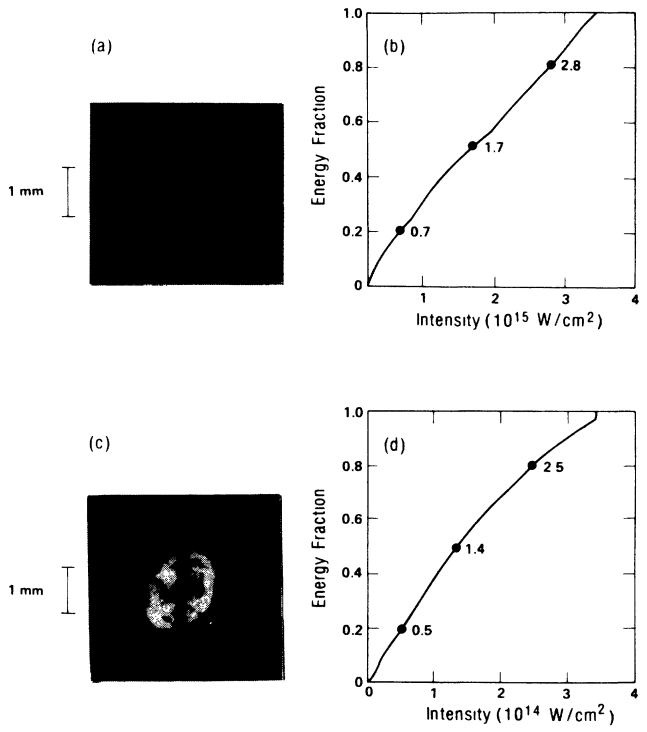

FIG. 5. X-ray images and inferred intensity distributions for (a) and (b) 2×10^{15} and (c) and (d) 1×10^{14} W/cm^2 irradiations of gold disks. Intensity distributions of the light were inferred assuming that the x-ray emission at few-keV energies is proportional to the incident intensity, then normalizing the distribution to correspond with the total incident energy.

seen, including, on some shots, portions of the 5×5 rectangular mask produced by the support framework for the 25-segment doubling crystal arrays. The sharpness and contrast of these structures indicates minimal effect from thermal smoothing, so we can be confident that the structures seen in x-ray emission represent the optical beam characteristics reasonably well. If we assume that the few-keV x-ray emission is roughly proportional to the locally absorbed energy flux over a moderate range of intensities, as suggested by calculations, we can use the emission intensity distribution to infer the laser-beam intensity distribution in the target plane. The results of this are shown in Fig. 5, next to each x-ray image. The film exposure curve has been taken into account, and the intensity axis has been normalized so that the integrated energy of the beam intensity distribution equals the measured total beam energy. The intensity spread is about a factor of 3–4 for the bulk of the delivered energy.

We obtained complete data sets for 1×10^{14} and 2×10^{15} W/cm^2, and time-resolved x-ray emission-pulse measurements at 3×10^{14} W/cm^2. Reproducibility of the data obtained was good, as discussed in more detail below.

IV. SOFT-X-RAY MEASUREMENTS AND ANALYSIS

In this section, we present the data and analysis for the two main soft-x-ray measurements: (1) the absolute broadband x-ray emission spectrum and (2) the time dependence of the sub-keV emission in selected energy bands. Analysis of the broadband x-ray spectrum occupies most of this section, since a subtle issue arose in this area: interpretation of broadband x-ray spectral measurements can be misleading if the spectrum being measured is not well known, particularly if it has specific structures that interact with the detector response functions. In the present experiment, the gold M-line emission could have interacted with the high-energy tails of the Dante channel responses to affect the inferred sub-keV spectrum for the high-intensity case. That such effects were probably important in this work is suggested by this analysis and also by recent measurements performed using the Nova laser,[22] where Dante was modified to contain channels that responded only to the above-1.5-keV emission from gold targets.[20] Also, high-resolution spectral measurements[8,9] performed at 0.35-μm wavelength showed that line emission from gold (especially M and O lines) can be significant and is not currently well modeled by LASNEX. As a result, the unfolding procedure normally used for measurements such as these[3,5,8] could be inaccurate. Therefore more detailed analysis was performed to ascertain the importance of these effects. The results of the present analysis differ only slightly from those obtained using the usual unfolding procedure,[3] giving us increased confidence in the measurements. The time-resolved sub-keV measurements are discussed and compared with calculations at the close of this section.

A. Overview of the analysis

Since the analysis is detailed, we present here only an overview of the procedure used. In broadband spectral measurements, uncertainty can arise from the detector response functions and their relationship to the spectrum being measured.[20] Therefore we wrote an analysis code DET to fold trial spectra with the Dante response functions and predict detector "signals."

Input spectra were generally obtained from LASNEX calculations with various model assumptions. However, DET permitted changing the input spectrum before folding so that sensitivity studies based on modeling uncertainties or results of related experiments could be performed. Two classes of spectral modifications were incorporated: (1) addition of one or two Gaussian "lines," each with adjustable central photon energy, peak amplitude, and FWHM; and (2) multiplication of the spectrum above a cutoff energy by an exponential factor, $\exp[-\alpha(h\nu-h\nu_0)]$, with adjustable cutoff energy $h\nu_0$ and slope α.

The predicted channel signals (S_p) were compared with the measured signals (S_m) using a reduced-χ^2 (χ_r^2) statistical analysis to obtain a quantitative assessment of the likelihood of a particular spectrum. By using trial spectra based on various LASNEX models, and also spectra with empirical shape adjustments based on related experiments, we evaluated the range of spectral shapes that could be consistent with the measured signals. Then we inferred quantitative uncertainty limits for the total- and sub-keV-conversion efficiencies. Further details of our

analysis are available elsewhere.[23]

The spectra and detector signals input to DET were normalized by either the incident or absorbed laser energy. The choice of normalizing energy is not an issue for the 1×10^{14}-W/cm^2 analysis, since the absorption was almost certainly $\approx100\%$. For the 2×10^{15}-W/cm^2 case, where the absorption is not known to be 100%, the choice of normalization is potentially important. Further, the issues are slightly different for calculations than for the experiment. For the data analysis, we can only normalize the measured Dante signals by the incident laser energy, since the absorption was not measured. The x-ray spectra and conversion efficiencies derived from fitting the experimental signals are thus normalized by the *incident laser energy,* and we use η_s^i and η_t^i to denote the soft- and total-x-ray conversions, respectively. Based on related experiments where absorption measurements were obtained,[4,5,8,9] the absorption in this experiment was likely to be 90–95 % for the 2×10^{15}-W/cm^2 case. However, the reference modeling yields about 80% absorption at 2×10^{15} W/cm^2 and, further, this absorption is somewhat sensitive to modeling details. Hence we wish to separate absorption and x-ray-emission processes to understand the x-ray measurements. To accomplish this, we have normalized the calculated emission by the calculated *absorbed energy.* There is a slight inconsistency in this procedure, but the error is only $\pm5\%$ if the experimental absorption is in the expected range, and therefore probably much less than other uncertainties associated with the measurements. We neglect this slight inconsistency in the analysis that follows, but restore the distinction when we return to infer x-ray conversion efficiencies in Sec. IV D.

B. Soft-x-ray-emission spectrum at high intensity

Figure 6 shows the LASNEX-calculated ($f_e=0.05$) spectrum for the 2×10^{15}-W/cm^2 case, and the results of folding the spectrum through the Dante response functions. The calculated spectrum corresponds with a total-x-ray conversion efficiency of $\eta_t=52\%$, and a "soft"-x-ray conversion efficiency ($h\nu\leq1.5$ keV) of $\eta_s=43\%$. The predicted signals are compared with the data by normalizing to the measured signal for each channel (S_p/S_m). A "perfect" prediction of the spectrum would result in $S_p/S_m=1/f_{\rm abs}$ for all channels, to within the uncertainty in the measured signals, where $f_{\rm abs}$ is the actual absorption fraction in the experiment. As noted above, the expected absorption fraction $f_{\rm abs}$ for the 2×10^{15}-W/cm^2 irradiations is about 90–95 %, and the total measurement uncertainties for the individual Dante signals are about 15%, so deviations in S_p/S_m smaller than 15–20 % might result from experimental uncertainties alone. From Fig. 6(b), we see deviations ranging over about $\pm25\%$ for the predicted signals derived from the reference LASNEX spectrum. The value of χ_r^2 for the reference spectrum is 1.5, which represents an acceptable fit, though possibly outside experimental errors.

In spite of this encouraging first-pass agreement between the modeling and the data, we were concerned about the uniqueness of the interpretation. We also considered possible spurious effects that could arise from (unmeasured) gold *M*-line emission near 2.5 keV, interacting with the high-energy Dante channel response lobes. Therefore we constructed and tested many additional trial spectra. We took two basic approaches: (1) examining changes of LASNEX-model parameters in those areas deemed most uncertain; and (2) optimizing the quality of the fit by using spectral adjustments based on related experiments.

Our LASNEX-model variations included changes in two key modeling features: electron transport and non-LTE radiation processes. Use of an electron-transport model based on flux-limited diffusion has usually been adequate to describe experimental behavior, but prediction of the required flux-limit value has been an area of repeated surprises.[3,5,17,18] Another area where the physics is considerably more complex than available models is that of

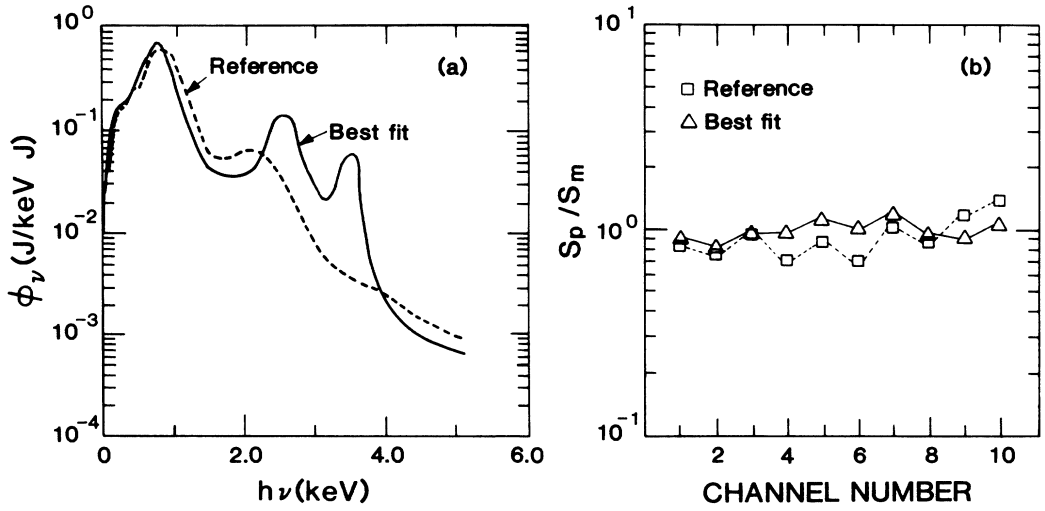

FIG. 6. LASNEX-calculated (reference, dashed line) and best-fit (solid line) x-ray spectra (a) for the 2×10^{15}-W/cm^2 case, and comparisons (b) with the measured signals. S_p/S_m is the ratio of the "predicted" signal to that measured, for each Dante channel.

the non-LTE atomic and x-ray emission physics. Both classes of physical processes affect the x-ray spectrum and also the total emission levels.

Our calculations with varying flux limit f_e showed some interactions between total emission level and spectral shape. With $f_e=0.05$, we obtained a nearly ideal fit to the integrated x-ray emission. However, using more-inhibited electron transport, with $f_e=0.03$, the spectrum became flatter and fell off more rapidly above 1 keV. As a result, even though the total emission calculated with $f_e=0.03$ was about 13% below that inferred from the measurements, the overall fit improved. Flux-limit values $f_e=0.02-0.07$ are consistent with the data.

Similar changes in emission level and spectral shape occur when the non-LTE emission opacity multiplier ϵ_r is varied. As mentioned in the modeling discussion (Sec. II A), we adopted, at the outset of this work, an emission opacity multiplier $\epsilon_r=0.7$ for the high-intensity case, to allow us to use affordable zoning. When we vary ϵ_r, we find a slight improvement in the fit using $\epsilon_r=0.85$ as a result of improved spectral shape. However, acceptable fit quality occurs for $\epsilon_r\simeq 0.6-1.2$.

To investigate possible effects of spectral shapes not produced by LASNEX modeling, we modified the reference $f_e=0.05$ LASNEX spectrum using prescriptions based on related experiments and our own concerns about spectral-shape sensitivity. Our empirical spectral modifications included enhancement of a single broad Gaussian line in the region of the gold M lines, addition of two Gaussians defined on the basis of M-line spectral data obtained in related 0.53-μm irradiations, and adjusting the slope of the x-ray spectral fall-off above 1.5 keV. We found no significant improvements from adjustments of the spectral fall-off, but obtained significant results from the M-line intensity variations.

The results of adjusting the x-ray emission in the region of the gold M lines (2–4 keV) are shown in Fig. 7. The curve shows the variation of χ_r^2 for the normalized fit as we vary the amplitude of a single added Gaussian peak of 0.5 keV FWHM, centered at 2.2 keV. The fit is considerably improved over the reference LASNEX spectrum by adding a Gaussian with amplitude about twice the reference LASNEX-predicted 2.2-keV flux.

Figure 7 also shows the point that results from adding a double-Gaussian constructed from high-resolution spectra obtained (using the Henway crystal spectrograph) in companion Novette experiments at 0.53-μm wavelength.[24] The two Gaussian peaks, centered at 2.6 and 3.4 keV, and of width 0.4 keV, were added at amplitudes taken from a measured 0.53-μm spectrum at the same $I\lambda^2$ as this 0.26-μm data. We consider use of this data plausible, since the M-line emission is most sensitive to the corona temperature, which should be about the same for irradiations at comparable energy, pulse width, and about the same $I\lambda^2$. The high-resolution spectrum and our two-Gaussian parametrization are shown in Fig. 8. An excellent fit is obtained, with a χ_r^2 reduction of about 0.5, suggesting that enhanced M-line emission is present in the 0.26-μm data at 2×10^{15} W/cm^2.

We combined the two most promising spectral adjustments found in the preceding analysis to construct a composite best-fit spectrum: the LASNEX spectrum using $f_e=0.03$ with an additional two-Gaussian component derived from the 0.53-μm measured M-line spectrum. This provided our overall best fit, decreasing χ_r^2 from 1.5 (10 degrees of freedom) to 0.42 (8 degrees of freedom), which is statistically significant. The best-fit spectrum is com-

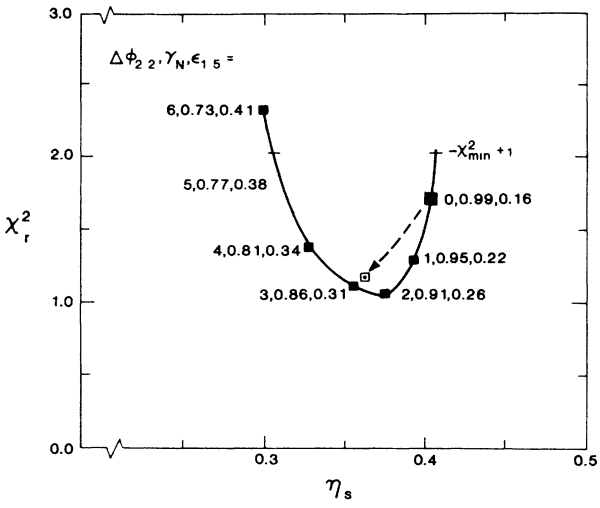

FIG. 7. Variation of χ_r^2 with η_s as the emission in the gold M-line region (near 2.5 keV) is varied. The curve is labeled with values of $\Delta\phi_{2\,2}$, the ratio of the amplitude of the added Gaussian (center 2.2 keV, width 0.5 keV) to the 2.2-keV flux predicted by the reference $f_e=0.05$ LASNEX spectrum (0.067 J/keV$-J_{abs}$). Also shown along the curve is the normalization constant γ_N required to minimize χ_r^2 for each of the points, and the fraction of the spectral energy that lies above 1.5 keV, $\epsilon_{1.5}$. The open square shows the result of using the M line spectrum taken from 0.53 μm irradiations at the same $I\lambda^2$ as these 0.26-μm experiments (see Fig. 8).

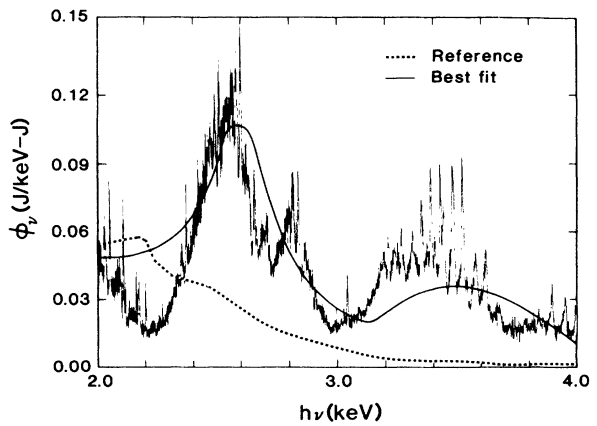

FIG. 8. Spectra in the region of the gold M lines. Data (structured curve) are the spectrum measured using a crystal spectrograph, for Novette irradiations of gold disks at 0.53 μm, 0.44 kJ, 1 ns, and 2×10^{14} W/cm^2. The dashed curve shows the reference $f_e=0.05$ LASNEX calculation, and the smooth curve shows the approximate, two-Gaussian parametrization of the data to obtain the open square point in Fig. 7.

pared with the original LASNEX $f_e=0.05$ reference spectrum in Fig. 6. The effect of the spectral modifications is to shift more of the emitted energy above 1.5 keV: the fraction of the total emission occurring above 1.5 keV ($\varepsilon_{1.5}$) increased from 15% for the reference spectrum to 25% (about 15% in the M lines) for the best fit.

C. Analysis of the soft-x-ray emission spectrum at low intensity

The low-intensity data have been analyzed using the same general approach discussed above, but the specific findings are quite different. For the 1×10^{14}-W/cm^2 intensity, electron transport is not inhibited when using flux limits $f_e\geq0.03$, since collisional mean free paths are short and plasma scalelengths are relatively long. Also, cooler temperatures in the corona at low intensity lead to negligible excitation of the gold M-line transitions that affected the high-intensity case. However, as in previous analysis[8] of low-intensity x-ray emission, we found discrepancies between the data and modeling.

The spectrum from the reference 1×10^{14}-W/cm^2 LASNEX calculation and a comparison with the measured channel signals are shown in Fig. 9. As expected, the calculated x-ray spectrum is softer than that for the high-intensity case (Fig. 6). Although N-line emission remains significant in the calculation, O-line emission can be seen above the continuum near 250 eV for this case, showing the importance of lower ionization states. The channel ratios S_p/S_m deviate from unity by up to 50%. The absolute (unnormalized) fit of the reference spectrum to the data is poor, with $\chi_r^2=2.7$, a value that would occur with only 0.5% probability if both model and measurements were correct. We can see immediately that the poor fit is partly caused by greater calculated emission than measured: when the fit is renormalized by multiplying the trial spectrum by a factor of 0.85, χ_r^2 is reduced to 1.5. Thus the calculation overestimates the total emission by about 15% at 1×10^{14} W/cm^2. This excess calculated emission is qualitatively consistent with the previously reported low-intensity emission discrepancy,[5] but the magnitude of the discrepancy is reduced here. In addition to this clear discrepancy in absolute emission level, there may be spectral shape discrepancies, since the S_p/S_m channel values still show systematic deviations from unity by $\pm20-30$%.

We examined many aspects of the LASNEX modeling, including numerical convergence and accuracy criteria, and various aspects of the laser absorption, electron transport, and non-LTE modeling. We found no simple model variations that appeared relevant to either the emission-level or spectral-shape discrepancies. Therefore we studied empirically spectral-shape discrepancies that might offer physical insight into possible modeling or experimental errors.

As in the high-intensity case, we constructed and tested trial spectra of various forms, partly motivated by high-resolution spectra of similar experiments,[6,8] and partly led by the discrepancies themselves. Two spectral regions appear troublesome: the O-line region, near 250 eV, and the region around the N lines and the spectrum roll-off, near 0.8–1.2 keV. Evidence for enhanced (greater-than-calculated) emission from the 250-eV region has been found in 0.35-μm experiments.[8,9] Here, we found that adding a Gaussian of 130-eV FWHM, centered at 230 eV, significantly improves the fit to the low-energy channels. Best fit was obtained by adding about 50% of the LASNEX-calculated 230-eV flux, which represents about 5% of the total emission.

We also found that the 0.8–1.2-keV spectral region could be fit slightly better using a combination of emission reduction near 0.8 keV and about the same amount of emission enhancement near 1.1 keV. Spectral adjustments in the 0.8–1.1-keV region were insensitive to the exact details, but the apparent need to shift some energy from 0.8 to 1.1 keV might point to miscalculation of an energy level or transition energy. A possible source of such a transition-energy shift is higher-than-calculated ionization, perhaps caused by high-intensity portions of

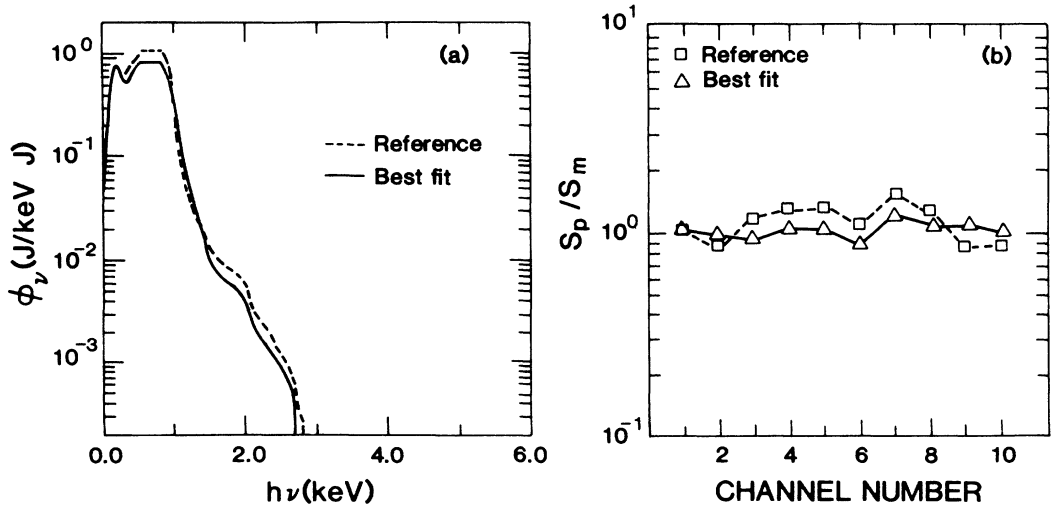

FIG. 9. (a) Spectra and (b) S_p/S_m for the 1×10^{14}-W/cm^2 case.

the beam spot. Better measurements in this spectral region are needed before definite conclusions can be drawn.

We have combined our two most successful individual fitting efforts for the low intensity case. Our best-fit spectrum for 1×10^{14} W/cm^2 is shown in Fig. 9, along with the reference spectrum. With the addition of a "line" at 230 eV, representing about 5% of the total x-ray emission, and the addition of roughly 3% of the total emission at 1.1 keV, the spectral shape fit is considerably improved. With both the renormalization and the two slight spectral-shape adjustments, we obtained an excellent fit, with $\chi_r^2=0.5$.

D. Inferred x-ray conversion efficiencies

Here, we use the results from the spectral studies above to determine x-ray conversion efficiencies and associated uncertainty limits. Figures 10 and 11 show composite plots of all our fitting results for the high- and low-intensity cases. The curves show χ_r^2 as a function of η_s^i, the soft-x-ray conversion efficiency relative to the incident laser energy. We take as the best value for the soft-x-ray conversion efficiency the value of η_s^i that minimizes χ_r^2 over the entire set of fitting results at each intensity. Shown on the plots are uncertainty limits based on the value of χ_r^2 that corresponds to 90% confidence interval for the appropriate number of degrees of freedom.

Certain systematic experimental uncertainties need to be taken into account to derive final error estimates. The analysis to this point has included the effects of uncertainties from shot-to-shot variations and channel-to-channel calibration. The remaining sources of uncertainty that must be considered are those that are systematic and could affect all the data. This includes uncertainties

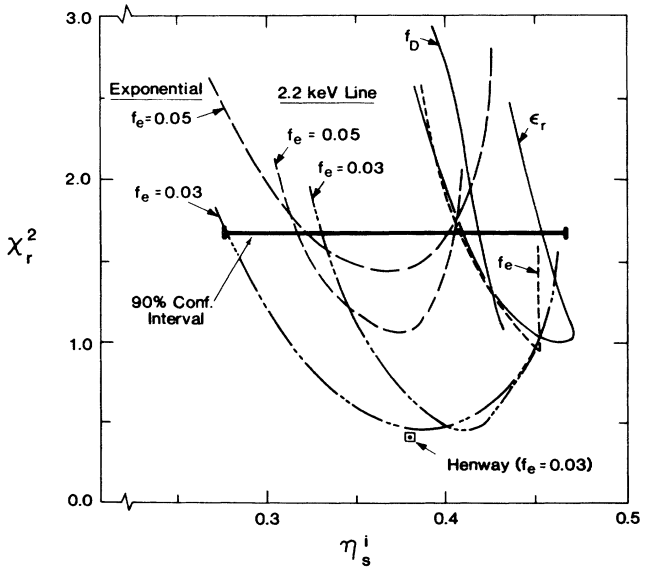

FIG. 10. Composite of all modeling and spectral variations for the 2×10^{15}-W/cm^2 case. Uncertainty limits on η_s^i are chosen such that χ_r^2 remains below the value associated with a 90% confidence level.

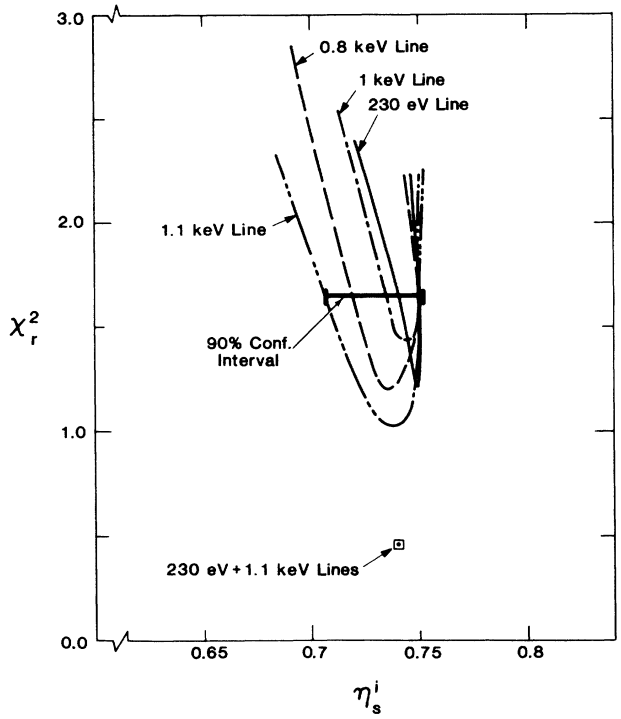

FIG. 11. Composite of all modeling and spectral variations for the 1×10^{14}-W/cm^2 case. Uncertainty limits on η_s^i are chosen such that χ_r^2 remains below the value associated with a 90% confidence level.

from the calibration of the incident laser energy measurement, the unmeasured absorption (mainly for the high-intensity point), and the unmeasured x-ray angular distribution. We have estimated these uncertainties, and take them into account by adding in quadrature an additional ±20% to the nonsystematic error bars resulting from the modeling and spectrum fitting. Table I summarizes the resulting conversion efficiencies and error limits.

E. Time dependence of the soft-x-ray emission

Figure 12(a) shows the incident laser pulse shape measured for a particular irradiation at 3×10^{14} W/cm^2 using a streak camera sampling a portion of the 0.26-μm laser light. Also shown is the smoothed fit used as input to calculations. The plots of Figs. 12(b) and 12(c) show the measured and calculated x-ray-emission pulses for photon energies of about 200 and 500 eV (adjusted along the time axis for best apparent fit, since the measurements were not absolutely timed with respect to the laser pulse). The emission pulse time dependence is mainly determined by the laser pulse shape. Agreement between calculation and experiment appears good on the pulse rise and over most of the duration. However, the measured x-ray-emission pulses for both x-ray energies are shorter than calculated and, in particular, the observed emission appears to decrease more rapidly than calculated. A similar discrepancy was previously reported at 0.53-μm wavelength.[5]

TABLE I. Total conversion efficiency (η_t') and sub-1.5-keV conversion efficiency (η_s') for 0.26-μm gold-disk irradiations, and estimated uncertainty limits.

	η_t'			η_s'		
		Limit			Limit	
	Best	Upper	Lower	Best	Upper	Lower
Low intensity (1×10^{14} W/cm^2)	0.72	0.87	0.58	0.72	0.87	0.58
High intensity (2×10^{15} W/cm^2)	0.52	0.69[a]	0.42	0.38	0.49	0.25[a]

[a]The upper limit for η_t', and the lower limit for η_s', in the high-intensity case, were determined by the $f_e=0.03$ calculation with an exponential tail adjustment. All other variations produced upper limits for η_t' no greater than 0.63 and lower limits for η_s' of 0.32 or greater.

The decay of the x-ray emission depends on the evolution of plasma temperatures and densities after the laser heating is removed. The fall-off of the x-ray emission is insensitive to some of the most-uncertain aspects of the calculations. Reasonable changes in the electron flux limit or the x-ray-emission opacity do not significantly alter the decay of the x-ray pulse.

One factor, however, that is significant in determining the cooling rate is the rate of hydrodynamic expansion of the corona. This is demonstrated by the 1D calculations shown in Fig. 12 for "flat" and for "spherical segment" geometries. The divergence of the blow-off plasma in the 1D spherical calculation reduces the plasma cooling time significantly. The 2D calculation shows slightly higher cooling rate, since it has greater coronal expansion than the 1D spherical geometry. However, even the full 2D calculation does not predict rapid enough cooling to match the experimental emission decay. The remaining discrepancy could be caused by miscalculation of one or more of these processes: the plasma cooling rate (either through hydrodynamic expansion or by conduction into dense matter), or, perhaps, the rates of free-bound emission processes in the expanding, cooling plasma.

V. HARD-X-RAY EMISSION AND HOT ELECTRON POPULATIONS

Hard-x-ray spectra indicate the behavior of the energetic electrons in the plasma. In most laser-plasma experiments at moderate-to-high intensities, energetic suprathermal electrons are generated by laser-plasma coupling instabilities in the corona. Much work,[25,26] using theory, simulations, and experiments, including recent work at 0.53- and 0.26-μm wavelengths,[27] has identified stimulated Raman scatter (SRS) below the quarter-critical density as an important hot-electron producer. Other processes that can generate suprathermal electrons at varying levels, depending on irradiation and plasma parameters, include resonance absorption[28] at the critical surface, and absolute SRS (Refs. 25 and 26) and the two-plasmon decay instability[26,29] at the quarter-critical surface. In this section, we analyze the measured hard-x-ray spectra and roughly characterize the heated-electron distributions.

Observed hard-x-ray spectra, shown in Fig. 13, imply relatively low coronal temperatures and very low suprathermal electron populations. At 1×10^{14}-W/cm^2 irradiance, no suprathermal tail is evident, and the observed thermal tail appears to be extremely soft, roughly as calculated. At 2×10^{15} W/cm^2, the spectrum shows a distinct suprathermal tail. The slope and fluence of the tail suggests a 28-keV electron population containing of order 0.1% of the incident energy. These implied levels of suprathermal electrons are negligible for the purposes of this work. They indicate the dominance of inverse bremsstrahlung absorption, and effective damping of collective plasma processes.

Even in calculations neglecting suprathermal electrons,

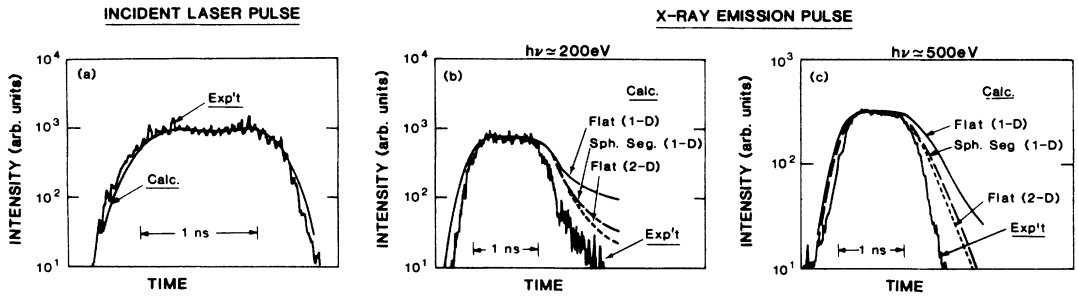

FIG. 12. (a) Temporal shapes for incident laser pulse and (b) and (c) x-ray emission pulses at 3×10^{14}-W/cm^2 intensity. Using the incident pulse shown as input, the calculated x-ray pulses are somewhat longer than those observed, mainly as a result of a considerably slower calculated decay.

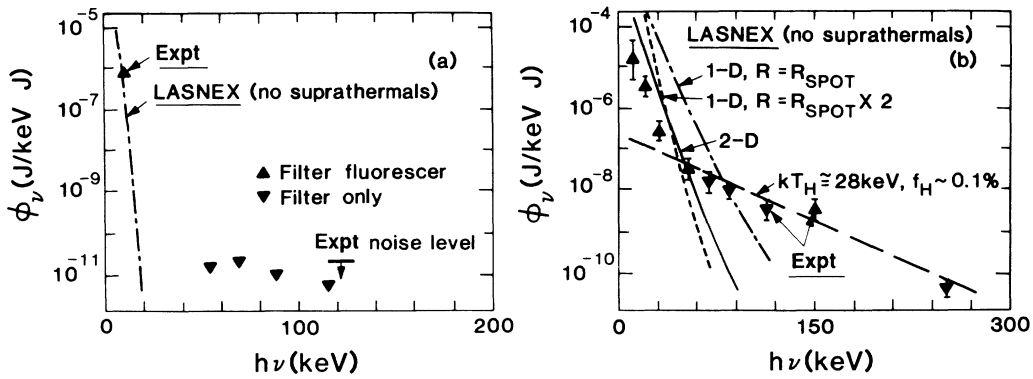

FIG. 13. Measured and calculated hard x-ray spectra for (a) 1×10^{14} and (b) 2×10^{15} W/cm^2, indicating cool coronas and very low suprathermal populations for this experiment.

a striking discrepancy is seen in the calculated excess of 10–50-keV x-ray emission for the high-intensity irradiations [Fig. 13(b)]. The sensitivity of this emission to small changes in corona temperature can be seen by comparing the results of the 1D and 2D calculations (which differ by about 10% in maximum corona temperature), or two 1D calculations with different spot sizes (which differ by about 20% in maximum temperature). LASNEX generates these x rays from the tail of the coronal "thermal" electrons, under the (perhaps oversimplified) assumption of a Maxwellian distribution. Since these electrons are at several kT_e, significant deviations from a Maxwellian could sharply reduce the electron populations in this energy range.

Such distribution-function alterations have been produced by nonlinear inverse bremsstrahlung[30] and transport.[31] Since the hard-x-ray spectrum is depressed so strongly, and calculations suggest that the hard-x-ray emission is not sensitive to thermal transport coefficients, an underpopulation of the electron tail by the laser absorption appears most likely. The high-energy portion of the electron distribution function is underpopulated when the absorption rate is substantially faster than the electron-electron collisional rates that populate the tail. The parameter that characterizes the amount of distortion of the distribution function is $Z(v_0/v_e)^2$, where Z is the average ion charge, v_0 is the electron oscillatory velocity in the applied laser field, and v_e is the electron thermal velocity. Thus the effect occurs most strongly for high-Z plasmas irradiated at high intensities, as in the 2×10^{15}-W/cm^2 case here. We estimate $Z(v_0/v_e)^2$ is about 0.4 for the high-intensity irradiations, a regime where this effect is predicted to occur. The electron distribution function might also affect and be affected by electron-ion collisions in high-Z plasmas.[32] More quantitative modeling of the predicted non-Maxwellian electron distribution effects could be a fruitful area for future research.

VI. SUMMARY AND CONCLUSIONS

In this work, we have examined the characteristics of x-ray emission from 0.26-μm laser-irradiated gold-disk targets, and considered some of the implications of this emission for the heating, expansion, and atomic processes in the plasma. We observed the absolute spectrum and time dependence of the soft x rays, and the broadband multi-keV emission spectrum. Probably the most important result of this work is this: the general improvements in laser-plasma coupling characteristics that have been previously reported at longer wavelengths and/or lower laser energies persist at 0.26-μm wavelength and kilojoule plasma energies. Laser-plasma coupling at 0.26-μm wavelength has been shown to be favorable at kilojoule energies, with very low suprathermal electron populations and efficient conversion of laser light into soft x rays.

We inferred suprathermal electron distributions at 2×10^{15} W/cm^2 with temperature about 28 keV, containing roughly 10^{-3} of the incident laser energy. These levels are completely negligible for the present work and for near-term ICF applications. We note, however, that larger laser systems and the resulting longer plasma scalelengths could lead to increased suprathermal electron production in the future, so it is important to continue to study and monitor the hot electron processes.

The x-ray conversion results of this work are summarized in the updated overview of x-ray conversion measurements, shown in Fig. 14. Recall that, since absorption measurements were not made in this experiment, comparing the conversion efficiencies inferred here with other measurements (some of which also did not include absorption measurements) in Fig. 14 could include a slight error that could be corrected, if necessary, using future absorption measurements. For this comparison, we have adjusted η_s^i using an assumed absorption of 95% for the 2×10^{15}-W/cm^2 data, obtaining $\eta_s=0.40$ and $\eta_t=0.55$. For our high-intensity data, we show in the figure both the total conversion efficiency η_t and the sub-1.5-keV conversion efficiency η_s to show the importance of the emission above 1.5 keV.

We have also included in the plot of Fig. 14 several other recent x-ray conversion measurements.[6,9,11,24] Careful inspection of the data reveals three trends: (1) the overall tendency for the conversion efficiency to decrease at increasing $I\lambda^2$, generally as calculated; (2) a tendency for measurements made with higher laser energy (and spot or target diameter) to yield higher x-ray conver-

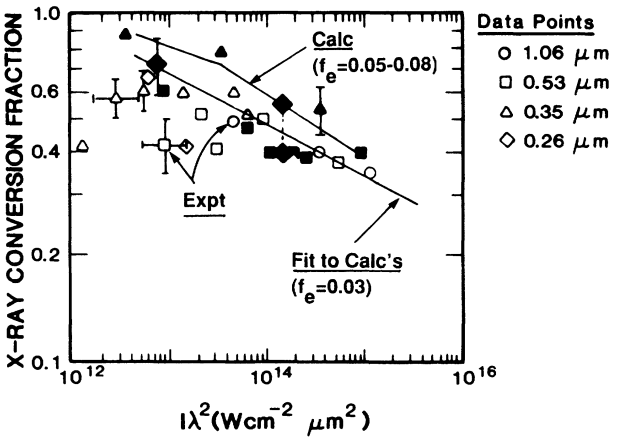

FIG. 14. Summary of x-ray conversion data, including results of this work (closed diamonds) and other 0.6–1-ns measurements reported to date. The scaling parameter chosen is $I\lambda^2$, based on fits to the modeling. For the 2×10^{15}-W/cm^2 data of this work, we have plotted both the total x-ray conversion fraction (η_t) and the sub-1.5-keV conversion fraction (η_s), assuming 95% absorption. The experimental data points have been plotted using open symbols (Refs. 3–6 and 9–11) for laser energies below 1 kJ, and solid symbols (Refs. 9, 24, and this work) for energies above 1 kJ. Recent LASNEX calculations, using $f_e=0.05$ and more rigorous treatment of numerical convergence of the atomic physics modeling, lie on the upper curve shown.

sion values at low intensities; and (3) higher conversion efficiencies from spherical targets irradiated by 24 beams (improved uniformity, larger spheres).[8,9] Note that measurements using small spherical targets irradiated by six beams[8,9] agree well with earlier planar experiments with small spot size.[5] Although only the first of these scaling trends is predicted by LASNEX calculations, the improved conversion using larger planar targets or large, uniformly irradiated spheres can be matched by calculations using less-inhibited electron thermal transport and somewhat improved modeling at low intensities. It is also noteworthy that the low-intensity rolloff seen in previous experiments[4,5] is less apparent in the recent large-target experiments, and thus the previously reported discrepancy, discussed above, now appears to be target-size (spot-size, laser-energy) dependent. The work currently available also strongly suggests that the low-$I\lambda^2$ discrepancy is mainly dependent upon intensity, and does not significantly degrade the predicted favorable scaling of x-ray conversion processes to 0.26-μm wavelength.

In general, we obtained good correspondence between LASNEX calculations and the measurements. The comparisons performed here support the general physical picture developed in the simulations of previous experiments.[3,5] LASNEX modeling with slight transport inhibition ($f_e=0.02-0.07$) reproduces many features of the experiments.

Some issues remain to be assessed and studied. The x-ray conversion efficiency data now suggest two scaling dependences that are not predicted by LASNEX calculations: target-size (or laser-energy) scaling at low intensities and differences between planar targets and uniformly irradiated spheres. At present, the differences between spherical and planar targets could be produced either by effects of the geometry change itself (which appears to be important for electron thermal transport in low-Z plasmas[17]) or by effects of greater beam uniformity achieved in the 24-beam spherical irradiations.[9] Certainly the beams used in this work were more structured than those of the Omega laser, which has been optimized for irradiation uniformity by the staff of the University of Rochester Laboratory for Laser Energetics. Another discrepancy seen here, namely, that LASNEX calculations overestimate the hard (10–50 keV) x-ray emission at high intensities by a large factor, confirms previous results,[5] and suggests that accounting for a sub-Maxwellian heated electron distribution[30] might be important. Finally, we have found here, as in previous work,[5] that the measured x-ray-emission pulse decays faster than calculated, indicating difficulties in modeling either the plasma cooling itself or the atomic physics in the cooling plasma. These areas need continued experimental and calculational work.

ACKNOWLEDGMENTS

We thank our Los Alamos colleagues, particularly W. Gula, M. Mahaffy, J. Norton, and J. Saltzman for valuable help in the use of LASNEX. We thank B. Bezzerides, S. R. Goldman, and P. D. Goldstone for valuable discussions. The support of D. Cartwright, D. Giovanielli, and S. Rockwood is appreciated. We thank our colleagues at Lawrence Livermore National Laboratory: D. Bailey, K. Estabrook, W. Kruer, M. Rosen, and L. Suter for valuable discussions; and R. P. Drake, J. Smith (Aracore, Inc.), and R. Turner for their contributions to the experiment. We appreciate the support of J. Emmett, E. Storm, and E. M. Campbell. We thank members of the Target Fabrication, Diagnostics, and Laser Operations groups at Livermore for their essential contributions. This work was performed under the auspices of the U.S. Department of Energy by Los Alamos National Laboratory under Contract No. W-7405-Eng-36 and by Lawrence Livermore National Laboratory under Contract No. W-7405-Eng-48.

[1]J. H. Nuckolls, Lawrence Livermore National Laboratory Report No. UCRL-50021-80, 1981 (unpublished), pp. 3-1–3-3.

[2]H. D. Shay, R. A. Haas, W. L. Kruer, M. J. Boyle, D. W. Phillion, V. C. Rupert, H. N. Kornblum, F. Rainer, V. W. Slivinsky, L. N. Koppel, L. Richards, and K. G. Tirsell, Phys. Fluids **21**, 1634 (1978).

[3]M. D. Rosen, D. W. Phillion, V. C. Rupert, W. C. Mead, W. L. Kruer, J. J. Thompson, and K. G. Tirsell, Phys. Fluids **22**, 2020 (1979).

[4]H. Nishimura, F. Matsuoka, M. Yagi, K. Yamada, S. Nakai,

G. H. McCall, and C. Yamanaka, Phys. Fluids **26**, 1688 (1983).

[5]W. C. Mead, E. M. Campbell, K. G. Estabrook, R. E. Turner, W. L. Kruer, P. H. Y. Lee, B. Pruett, V. C. Rupert, K. G. Tirsell, G. L. Stradling, F. Ze, C. E. Max, M. D. Rosen, and B. F. Lasinski, Phys. Fluids **26**, 2316 (1983).

[6]T. Mochizuki, T. Yabe, K. Okada, M. Hamada, N. Ikeda, S. Kiyokawa, and C. Yamanaka, Phys. Rev. A **33**, 525 (1986).

[7]K. Eidmann, T. Kishimoto, P. Herrmann, J. Mizui, R. Pakula, R. Sigel, and S. Witkowski, Lasers Part. Beams **4**, 521 (1986).

[8]W. C. Mead, S. V. Coggeshall, S. R. Goldman, E. K. Stover, P. D. Goldstone, J. Cobble, A. Hauer, G. Stradling, J. M. Kindel, L. Montierth, M. C. Richardson, O. Barnouin, P. Jaanimagi, F. Marshall, R. Marjoribanks, R. L. Kauffman, H. N. Kornblum, and B. F. Lasinski, *Laser Interaction and Related Plasma Phenomena* (Plenum, New York, 1986), Vol. 7, p. 723.

[9]P. D. Goldstone, S. R. Goldman, W. C. Mead, J. A. Cobble, G. Stradling, R. H. Day, A. Hauer, M. C. Richardson, R. S. Majoribanks, P. A. Jaanimagi, R. L. Keck, F. J. Marshall, W. Seka, O. Barnouin, B. Yaakobi, and S. A. Letzring, Phys. Rev. Lett. **59**, 56 (1987).

[10]K. Eidmann and T. Kishimoto, Appl. Phys. Lett. **49**, 377 (1986); P. Alaterre, H. Pepin, R. Fabbro, and B. Faral, Phys. Rev. A **34**, 4184 (1986).

[11]R. Kodama, K. Okada, N. Ikeda, M. Mineo, K. A. Tanaka, T. Mochizuki, and C. Yamanaka, J. Appl. Phys. **59**, 3050 (1986).

[12]G. D. Tsakiris, P. Herrmann, R. Pakula, S. Schmalz, R. Sigel, and S. Witkowski, Europhys. Lett. **2**, 213 (1986); K. Okada, T. Mochizuki, N. Ikeda, M. Hamada, M. Mineo, R. Kodama, and C. Yamanaka, J. Appl. Phys. **59**, 2332 (1986); T. Mochizuki, T. Yabe, H. Azechi, K. A. Tanaka, T. Boehly, N. Miyanaga, H. Nishimura, S. Ido, M. Yamanaka, K. Nishihara, T. Norimatsu, T. Jitsuno, M. Nakatsuka, K. Mima, S. Nakai, C. Yamanaka, R. Sigel, G. D. Tsakiris, K. Eidmann, P. Herrmann, R. Pakula, P. Sachsenmaier, S. Sakabe, and S. Witkowski, in *Plasma Physics and Controlled Nuclear Fusion Research,* Proceedings of the Eleventh International Conference on Plasma Physics and Controlled Nuclear Fusion Research, Kyoto, Japan, 1986 (I.A.E.A., Vienna, 1987), Vol. 3. p. 25.

[13]R. F. Schmalz, J. Meyer-ter-Vehn, and R. Ramis, Phys. Rev. A **34**, 2177 (1986).

[14]S. R. Goldman and W. C. Mead, Nucl. Fusion **26**, 813 (1986).

[15]R. L. Kauffman, R. P. Drake, R. E. Turner, B. F. Lasinski, G. Tirsell, W. C. Mead, and E. Stover, Bull. Am. Phys. Soc. **29**, 1183 (1984); E. K. Stover, W. C. Mead, R. L. Kauffman, R. E. Turner, B. F. Lasinski, and J. Smith, *ibid.* **29**, 1377 (1984).

[16]G. B. Zimmerman, Lawrence Livermore National Laboratory Report No. UCRL-75881, 1974 (unpublished); G. B. Zimmerman and W. L. Kruer, Comments Plasma Phys. Controlled Fusion **2**, 51 (1975); R. M. More and G. B. Zimmerman, Lawrence Livermore National Laboratory Report No. UCRL-50021-79, 1980 (unpublished), pp. 3-66–3-72.

[17]B. Yaakobi, T. Boehly, P. Bourke, R. S. Craxton, J. Delettrez, J. M. Forsyth, R. D. Frankel, L. M. Goldman, R. L. McCrory, M. C. Richardson, W. Seka, D. Shvarts, and J. M. Soures, Opt. Commun. **39**, 175 (1981); T. J. Goldsack, J. D. Kilkenny, B. J. MacGowan, P. F. Cunningham, C. S. Lewis, M. H. Key, and P. T. Rumsby, Phys. Fluids **25**, 1634 (1982); A. Hauer, W. C. Mead, O. Willi, J. D. Kilkenny, D. K. Bradley, S. D. Tabatabaei, and C. Hooker, Phys. Rev. Lett. **53**, 2563 (1984).

[18]W. C. Mead, E. M. Campbell, W. L. Kruer, R. E. Turner, C. W. Hatcher, D. S. Bailey, P. H. Y. Lee, J. Foster, K. G. Tirsell, B. Pruett, N. C. Holmes, J. T. Trainor, G. L. Stradling, B. F. Lasinski, C. E. Max, and F. Ze, Phys. Fluids **27**, 1301 (1984).

[19]H. G. Ahlstrom, L. W. Coleman, F. Rienecker, Jr., and V. W. Slivinsky, J. Opt. Soc. Am. **68**, 1731 (1978).

[20]H. N. Kornblum, R. L. Kauffman, and J. A. Smith, Rev. Sci. Instrum. **57**, 2179 (1986).

[21]N. M. Ceglio, H. Medecki, R. L. Kauffman, and D. G. Stearns, Lawrence Livermore National Laboratory Report No. UCRL-50021-84, 1985 (unpublished), pp. 5-51–5-55.

[22]R. L. Kauffman, M. D. Cable, H. N. Kornblum, and J. A. Smith, Lawrence Livermore National Laboratory Report No. UCRL-50021-85, 1986 (unpublished), pp. 4-5–4-8.

[23]W. C. Mead, E. K. Stover, R. L. Kauffman, H. N. Kornblum, and B. F. Lasinski, Los Alamos National Laboratory Report No. LA-UR-87-2548, 1987 (unpublished).

[24]E. M. Campbell, R. P. Drake, R. E. Turner, D. W. Phillion, W. L. Kruer, B. F. Lasinski, C. L. Wang, K. G. Estabrook, and C. W. Hatcher, in Fourteenth Annual Anomalous Absorption Conference, Charlottesville, 1984 (unpublished); R. L. Kauffman, R. E. Turner, B. F. Lasinski, R. P. Drake, J. A. Smith, W. C. Mead, and E. K. Stover, Lawrence Livermore National Laboratory Report No. UCRL-50021-84, 1985 (unpublished), pp. 5-31–5-35.

[25]C. S. Liu, M. N. Rosenbluth, and R. B. White, Phys. Fluids **17**, 121 (1974); D. W. Forslund, J. M. Kindel, and E. L. Lindman, *ibid.* **18**, 1002 (1975); **18**, 1017 (1975); W. Manheimer and H. Klein, *ibid.* **17**, 1889 (1974); B. I. Cohen, A. N. Kaufman, and K. M. Watson, Phys. Rev. Lett. **29**, 581 (1972); W. L. Kruer, K. G. Estabrook, B. F. Lasinski, and A. B. Langdon, Phys. Fluids **23**, 1326 (1980).

[26]H. Figueroa, C. Joshi, H. Azechi, N. A. Ebrahim, and K. Estabrook, Phys. Fluids **27**, 1887 (1984), and references therein.

[27]R. E. Turner, K. Estabrook, R. L. Kauffman, D. R. Bach, D. W. Phillion, B. F. Lasinski, E. M. Campbell, W. L. Kruer, and E. A. Williams, Phys. Rev. Lett. **54**, 189 (1985); R. P. Drake, R. E. Turner, B. F. Lasinski, K. G. Estabrook, E. M. Campbell, C. L. Wang, D. W. Phillion, E. A. Williams, and W. L. Kruer, *ibid.* **53**, 1739 (1984).

[28]E. J. Valeo and W. L. Kruer, Phys. Rev. Lett. **33**, 750 (1974); J. M. Kindel, K. Lee, and E. L. Lindman, *ibid.* **34**, 134 (1975).

[29]H. A. Baldis, J. C. Samson, and P. B. Corkum, Phys. Rev. Lett. **41**, 1719 (1978); A. B. Langdon, B. F. Lasinski, and W. L. Kruer, *ibid.* **43**, 133 (1979).

[30]A. B. Langdon, Phys. Rev. Lett. **44**, 575 (1980).

[31]J. R. Albritton, Phys. Rev. Lett. **50**, 2078 (1983).

[32]R. M. More, Lawrence Livermore National Laboratory Report No. UCRL-84991, 1981 (unpublished).

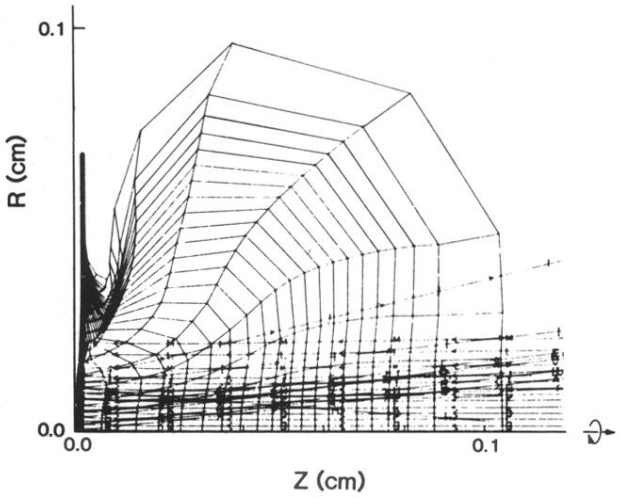

FIG. 2. Snapshot of 2D LASNEX calculation at the time of the peak of the laser pulse for $\lambda_L = 0.26\ \mu$m, $\tau_L = 1$ ns, $E_L = 1.3$ kJ, and $I_L = 2 \times 10^{15}$ W/cm^2, using $f_e = 0.05$. Lagrangian mesh and laser rays (incident from the right) are shown. Remnant of the original disk target is seen at the left. Plasma plume expansion shows divergence of the flow away from the laser spot.

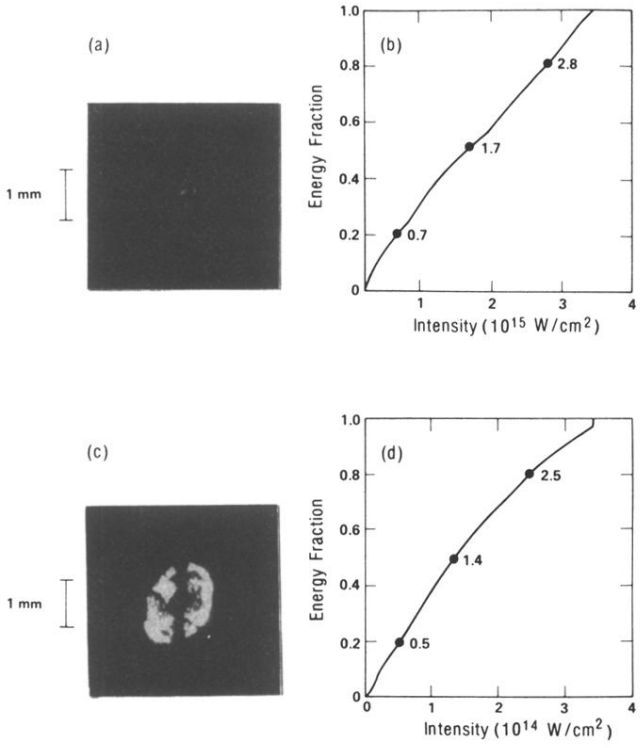

FIG. 5. X-ray images and inferred intensity distributions for (a) and (b) 2×10^{15} and (c) and (d) 1×10^{14} W/cm^2 irradiations of gold disks. Intensity distributions of the light were inferred assuming that the x-ray emission at few-keV energies is proportional to the incident intensity, then normalizing the distribution to correspond with the total incident energy.